

# Multiscale-engineered ferroelectric ceramics exhibiting superior electrocaloric performance

Received: 17 March 2025

Accepted: 1 September 2025

Published online: 03 October 2025

 Check for updates

Xiaowei Wei<sup>1,6</sup>, Kun Zeng<sup>1,6</sup>, Xiaoming Shi<sup>1,3,6</sup>, Gengguang Luo<sup>4</sup>,  
Zhengqian Fu<sup>1,2</sup>, Houbing Huang<sup>1,3</sup>✉, Guangzu Zhang<sup>1,4</sup>, Bing Li<sup>1</sup>,  
Xiang Lv<sup>1</sup>✉ & Jiagang Wu<sup>1,5</sup>✉

Electrocaloric effect referring to reversible temperature change ( $\Delta T$ ) under electrical excitation provides a promising alternative for next-generation thermal management. The  $\Delta T$  essentially derives from the polarization change of polar system. However, conventional engineering hardly synchronizes large and flexible polarization change, so that large  $\Delta T$  and high electrocaloric strength cannot realize concurrently. Herein, we propose a novel design strategy of multiscale engineering to boost the polar entropy of system, by which the large and flexible polarization change can be offered synchronously, availing large  $\Delta T$  under a low driving field. The envision is validated in a heterogeneous Ba $(\text{Ti}_{1-x}\text{Sn}_x)\text{O}_3$  system, where the different Ba $(\text{Ti}_{1-x}\text{Sn}_x)\text{O}_3$  granules are mixed to enhance polarization heterogeneity of system. A large  $\Delta T$  of 1.5 K and a high electrocaloric strength of 0.375 K mm kV $^{-1}$  are achieved under a low driving field of 40 kV cm $^{-1}$ . Meanwhile, the substantial  $\Delta T$  of more than 1.2 K is maintained within 30–50 °C. Our strategy provides a new paradigm for engineering electrocaloric material properties and can be expected for the design of other high-performance ferroelectrics.

Escalating climate and energy issues make it urgent to develop new cooling technologies with eco-friendliness and high efficiency. The electrocaloric (EC) effect, which elicits a reversible isothermal entropy change ( $\Delta S$ ) or adiabatic temperature change ( $\Delta T$ ) through the easy application and removal of an electric field ( $E$ ), presents a promising solution<sup>1–6</sup>. The EC effect essentially derives from the polarization change of the polar system<sup>3</sup>. Among various dielectrics, the polarization of perovskite-type ferroelectric ceramics is readily changed; that is, two polar states can be converted by a relatively low  $E$ . Therefore, ferroelectric ceramics are widely investigated for EC refrigeration.

In ferroelectric ceramics, the polarization changes as the phase structure changes, e.g., ferroelectric–ferroelectric (FF) or

ferroelectric–paraelectric (FP) phase transition<sup>7</sup>. The FP transition, where the crystallographic structure transforms most, possesses the largest polarization change, leading to a large  $\Delta T$ . However, the FP transition of normal ferroelectrics always happens at the temperature (i.e., Curie temperature  $T_C$ ) that is much higher than room temperature (RT), and the obtained  $\Delta T$  is accompanied by a narrow temperature span, which limits their application (case 1 in Fig. 1). To meet the RT cooling requirement, the long-standing approach focused on chemical substitution<sup>8–14</sup>.

As one of the most typical lead-free ferroelectric materials, EC effect in BaTiO<sub>3</sub> (BTO)-based ferroelectric ceramics has been extensively studied, and it is noteworthy that B(Ti $^{4+}$ )-site substitution plays a

<sup>1</sup>College of Materials Science and Engineering, Sichuan University, Chengdu, China. <sup>2</sup>State Key Laboratory of High Performance Ceramics and Superfine Microstructures, Shanghai Institute of Ceramics, Chinese Academy of Sciences, Shanghai, China. <sup>3</sup>Advanced Research Institute of Multidisciplinary Science, Beijing Institute of Technology, Beijing, China. <sup>4</sup>School of Integrated Circuits, Engineering Research Center for Functional Ceramics MOE and Wuhan National Laboratory for Optoelectronics, Huazhong University of Science and Technology, Hubei, China. <sup>5</sup>College of Physics, Sichuan University, Chengdu, China. <sup>6</sup>These authors contributed equally: Xiaowei Wei, Kun Zeng, Xiaoming Shi. ✉e-mail: [bhuang@bit.edu.cn](mailto:bhuang@bit.edu.cn); [lxixiang@scu.edu.cn](mailto:lxixiang@scu.edu.cn); [msewujg@scu.edu.cn](mailto:msewujg@scu.edu.cn)

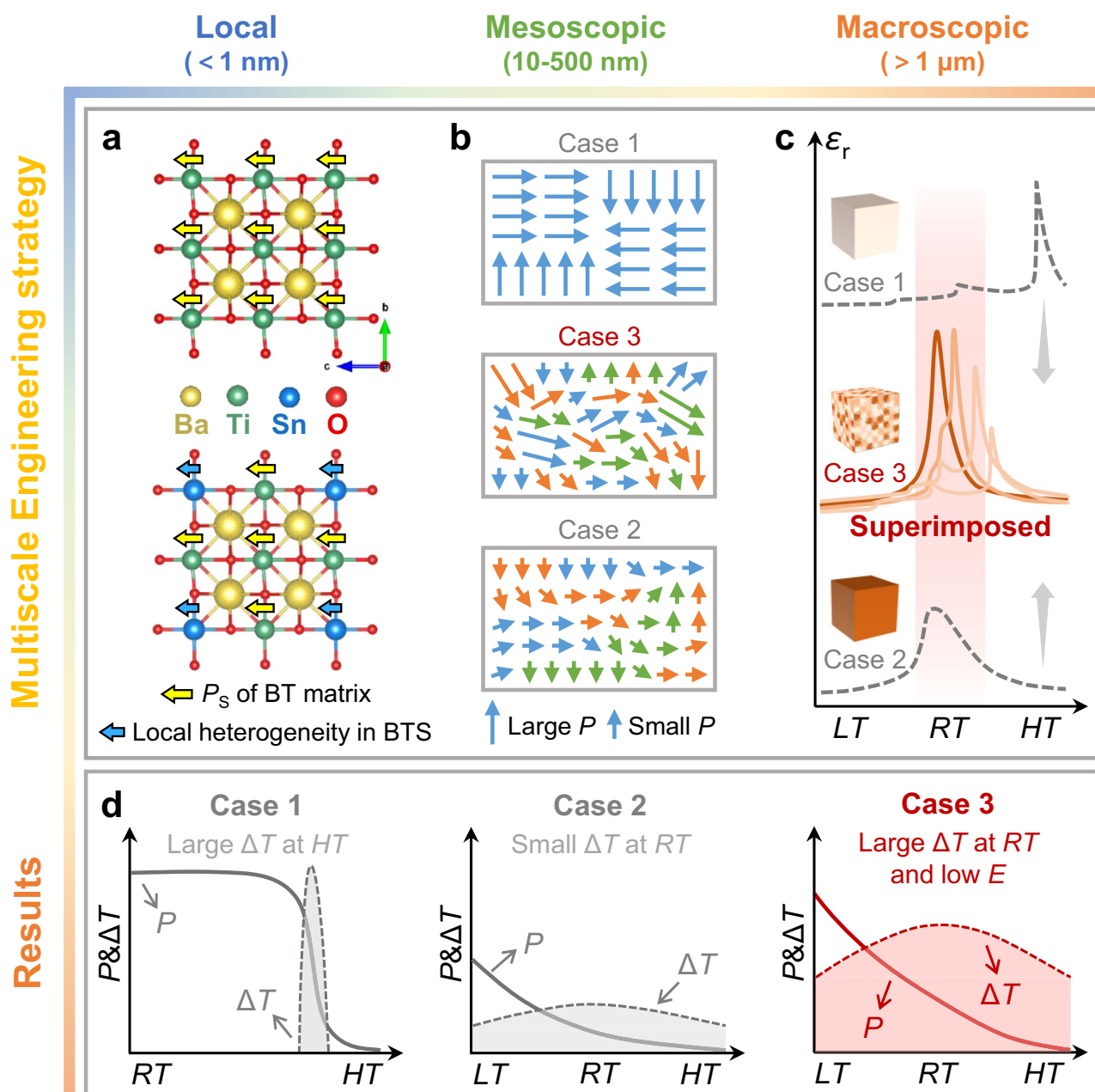


**Fig. 1 | Schematic illustration of EC property engineering in ferroelectric ceramics.** **a–c** Multiscale engineering strategy employed in this work, including (a) local scale, (b) mesoscopic scale, and (c) macroscopic scale, respectively. **d** Typical EC engineering strategies and their corresponding EC performances. The arrows in (a) refer to ferroelectric spontaneous polarization  $P_s$  on a local scale, where Sn doping induces atomic-scale heterogeneity and disrupts the long-range order of polarization. The arrows in (b) refer to mesoscopic average polarization  $P$ . The length of arrows represents the magnitude of polarization, while the colored arrows indicate polarization from various phases. Despite the heterogeneity on the

local scale, the traditional doping in individual composition causes relatively uniform polarization intensity on the mesoscopic scale, as seen in cases 1 and 2. In contrast, our strategy in case 3 designs to maintain significant polarization differences on the mesoscopic scale. The cubes inserted in (c) refer to ceramics with different doping concentrations. The light color represents the low doping, and the dark color represents the high doping. The solid and dashed lines in (d) describe the evolution of temperature-dependent polarization ( $P$ ) and the consequent  $\Delta T$  variation.  $RT$ ,  $LT$ , and  $HT$  refer to room temperature, below and above room temperature, respectively.

crucial role, due to its effective engineering on phase transition behavior<sup>7,15</sup>. For B-site substitution, the most utilized cations are valence-stable  $Zr^{4+}$ <sup>10,12,16</sup>,  $Hf^{4+}$ <sup>8</sup>, and  $Sn^{4+}$ <sup>9,17–19</sup>, which show similar ionic radii and the same valence as  $Ti^{4+}$ . Among them, Sn exhibits the most significant modulation on local heterogeneity and electrical properties<sup>20–22</sup>, and the  $Ba(Ti_{1-x}Sn_x)O_3$  (BTSx) system has hence received extensive attention. Via precisely regulating the critical Sn content ( $x=0.105$ ), a high value of  $\Delta T=0.61\text{ K}@20\text{ kV cm}^{-1}$  was reported by Luo<sup>17</sup>, followed by Zhang et al.<sup>18</sup> further modified the diffuse phase transition and turned BTSx into relaxor ferroelectrics

( $x=0.12$ ) to expand EC response. The diffusion behavior can effectively widen the temperature span, however, the high doping concentration in the Ti-site severely impairs the ferro-activity<sup>23</sup>. Therefore, despite a broadened phase transition temperature range, in reality, BTO-based ceramics exhibit relatively weak inherent polarization when they transition into a relaxor state, thereby compromising the EC performance (case 2 in Fig. 1). Many researchers imposed high driving fields to induce large  $\Delta T$ , but the high  $E$  is normally accompanied by a low EC strength ( $\Delta T/\Delta E$ ), i.e., reduced EC efficiency. Therefore, a better strategy toward superior EC performance is needed.

In principle, a system with both large and flexible polarization change (Figs. S1 and S2) can yield a sizable  $\Delta T$  by a relatively low  $E$ . Such a characteristic means the necessary polarization gradients (Fig. S1) in the system. Herein, we design a multiscale engineering to realize the polarization gradients, as depicted in case 3 in Fig. 1. Primarily, Sn was chosen for an atom-scale engineering [Fig. 1a, Figs. S3 and S4]. As for the BTSx system, the polarization can be directly determined by the concentration of Sn doping. In the low-Sn composition of BTS0.03, large and robust polarization is present due to the stable ferroelectric phases around RT. While in high-Sn composition of BTS0.12, polarization reduces in strength, but it becomes much flexible due to the flattened energy profile of multiphase coexistence (Figs. S5 and S6). Therefore, mesoscopic polarization state differs between BTSx compositions (Fig. 1b). To achieve the desired EC properties, i.e., large  $\Delta T$  by a low driving  $E$ , we further design the system with three-dimensionally connected macroscopic chemical heterogeneity. As noted in case 3 in Fig. 1c, the macroscopic chemical heterogeneity gathers multiple FF and FP phase transitions around the RT region. In such a system, various polarization states that come from different BTSx compositions coexist on the mesoscopic scale, boosting the polar entropy at zero field. Additionally, the three-dimensional (3D) connection forms interim regions that bridge different polarization states and introduce interfacial energy. This interfacial energy would compete with the bulk energy of the matrix, thereby lowering the Landau energy barrier between different phases (Fig. S2)<sup>24,25</sup>. Therefore, the large and flexible polarization change can be offered synchronously, favoring large  $\Delta T$  with low driving field (Fig. 1d).

## Results

### Ceramic materials design

To experimentally realize the proposed three-dimension-connected chemical heterogeneity, we synthesized the ceramics via a “granule-mixing” method<sup>26</sup>. The schematic can be seen in Fig. S7. Firstly, BTSx ( $x = 0.03, 0.06, 0.09, 0.12$ ) individual powders were prepared by the conventional solid-state reaction method (see “Methods” section). Then, four post-calcinated powders were separately granulated by adding polyvinyl alcohol (PVA) solution (Step 1). The granulation is a necessary process for the designed multiscale heterogeneity. To possibly control the subsequent sintering diffusion at the same level, the obtained granules were further sieved to filter the uniform granules, and a moderate size of 400  $\mu\text{m}$  was picked up (Step 2, Fig. S8). The 400  $\mu\text{m}$  granules of four individual compositions were well mixed together with the mass percentage of 1:1:1:1 and pressed into disks to fabricate a ceramic sample (Step 3). The nominal formula of the mixture is 25 wt% (BTS0.03 + BTS0.06 + BTS0.09 + BTS0.12), and we abbreviated it as BTS-M.

### Electrocaloric performance

The EC effect essentially relates to the reversibility of polarization upon the application and removal of  $E$ . Thus, a high maximum polarization ( $P_{\max}$ ) and a low remanent polarization ( $P_r$ ) are expected to obtain a large reversible polarization change ( $\Delta P$ ,  $\Delta P = P_{\max} - P_r$ ). Figs. S9–S12 demonstrate the temperature-dependent bipolar and unipolar hysteresis ( $P$ - $E$ ) loops. The temperature-dependent  $P_{\max}$  changes differently under different waveforms (i.e., consistent decrease with bipolar wave while phase transition-associated increase with unipolar wave, Fig. S13), but  $\Delta P$  shares a similar tendency and values, which reflects the real reversible polarization. In contrast to BTS0.03, BTS0.06, and BTS0.09 with sharp phase transitions, BTS0.12 and BTS-M maintain the relatively stable  $\Delta P$  within the tested temperature range, implying the broad EC temperature span.

The EC performance of BTS-M and four individual samples was then directly assessed by a modified heat flux sensor, and the detailed information about the measurement was provided in Figs. S14–16 and Table S2. We first tested the EC responses at RT with the continuously

changed  $E$ , where the exothermic and endothermic peaks both increase with the rising fields, and the temperature-dependent variation was subsequently measured under 40  $\text{kV cm}^{-1}$  (Figs. S17–20, Table S3). To verify the reproducibility of EC performance, we collected the EC signals of BTS-M from three cycles of heating and cooling processes (Figs. S21 and S22, Table S4). Within 25–60 °C, multiple FF and FP transitions from individual compositions were gathered due to the mixed BTSx granules. The integration of multiple phase transitions not only boosts the polar entropy of the system, which helps to produce a large  $\Delta T$ , but also widens the EC temperature window of BTS-M. As seen in Fig. 2a–e, BTS0.03, BTS0.06, and BTS0.09 show sharp phase transitions, the tendency of which is similar to their  $\Delta P$  variation. Although BTS0.12 and BTS-M are close in  $\Delta P$  value, BTS-M actually shows higher  $\Delta T$  values than BTS0.12 in direct measurement. Such a difference can be explained based on polarization dynamics (Fig. S13). From Fig. 2e,  $\Delta T$  of BTS-M shows an arch-like variation within 20–60 °C, and the maximum value reaches -1.55 K at 40 °C. The substantial  $\Delta T$  of more than 1.2 K is maintained within 30–50 °C. Such performance is also better than the average of four individual responses (Fig. 2f). Especially around 35 °C and 40 °C, where the superimposed number of phase transitions reaches the maximum (Fig. S5e),  $\Delta T$  increased by 34% and 26%, respectively. The enhancement in  $\Delta T$  value just verified the effectiveness of our designed heterogeneity on engineering EC performance, that is, boosting the polar entropy of the sample. For practical applications,  $\Delta T/\Delta E$  is also a worthy parameter that impacts the efficiency of the final prototype, so achieving both a large  $\Delta T$  and a high  $\Delta T/\Delta E$  is desired. In Fig. 2g, h, we reviewed the EC performance of representative ferroelectric ceramics. Encouragingly, within the field range of lower than 100  $\text{kV cm}^{-1}$ , BTS-M shows a relatively large  $\Delta T$  while a high  $\Delta T/\Delta E$  at 40 °C. Such superior EC performance indicates the successful implementation of a multiscale engineering strategy in the BTS-M system.

### Macroscopic heterogeneity

The superior EC performance fundamentally associates with the designed chemical heterogeneity. Therefore, the phase structure of BTS-M and individual samples was characterized (Figs. S23 and S24). The enlarged X-ray diffraction (XRD) patterns of BTS-M reveal abnormal peak splitting, which is attributed to diffraction of regions with different lattice parameters<sup>27</sup>. This finding confirms the existence of heterogeneity in BTS-M. Fig. 3a shows the surface morphology of BTS-M over the largest possible area. The sample features notably irregular grains and a few pinholes around the Sn-poor regions (the formation of pinholes was discussed in Fig. S25, and the variation of grain size was analyzed in Fig. S26). The EDS images show extensive inhomogeneity of Sn throughout the BTS-M, independently of grain size or location within grains, which corroborates the abnormally split peaks in XRD results. Fig. 3b contrasts the EDS spectra collected from Sn-poor and Sn-rich regions, where Sn is distinctly deficient in the Sn-poor region (Figs. S27 and S28). The detected atomic percentages of Sn in Sn-poor and Sn-rich regions are 0.69% and 2.5%, respectively (Fig. 3c). The measured deviation in Sn content (271%) fluctuates around the theoretical difference between BTS0.03 and BTS0.12 (300%), demonstrating the interdiffusion of Sn (Fig. S29). In theory, the doped Sn has formed stable solid solutions with the  $\text{BaTiO}_3$  matrix after calcination (1200 °C) (Fig. S30). Whereas, the mixing of BTSx granules brings additional chemical gradients in the system and drives Sn diffusion upon sintering (1380 °C). We observed the uneven Sn distribution from two-dimensional images, but it is conceivable that the Sn diffusion practically happens in three dimensions, leading to the formation of three-dimensionally connected chemical heterogeneity in BTS-M.

The large-scale inhomogeneity implies the conceivable chemical fluctuations inside one single grain. Raman spectroscopy, a powerful technique for detecting the local structure and symmetry, is further

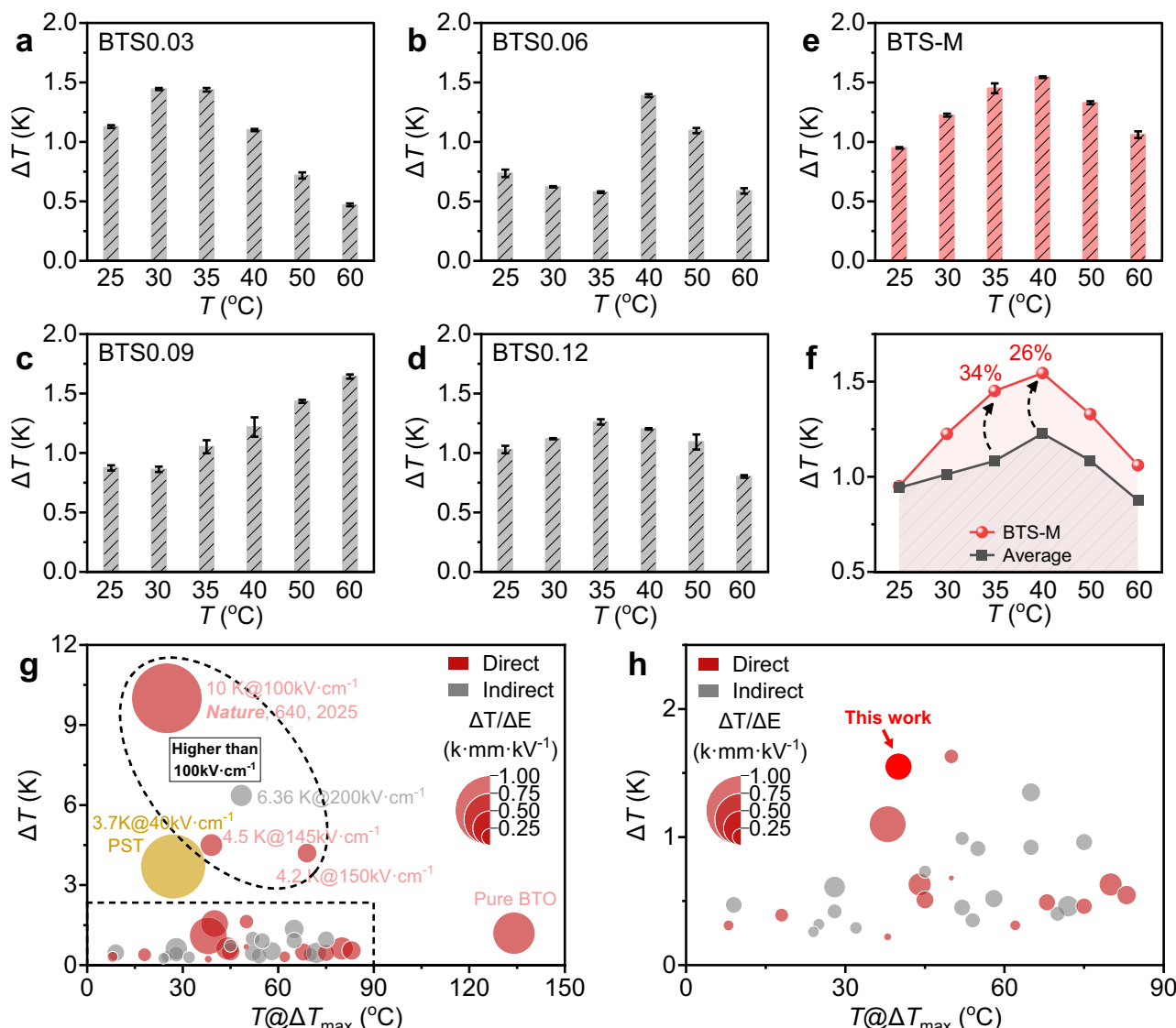


**Fig. 2 | EC performance of BTS-M.** **a–e** Direct EC results of individual and BTS-M samples measured under  $40 \text{ kV}\cdot\text{cm}^{-1}$  electric field. **f** Comparison of EC performance between BTS-M and the average of individual samples. **g** The comparison of EC

performance between the reported materials and BTS-M based on Table S1. The region marked by the dashed box is enlarged in **(h)**.

performed on a single grain to study the local chemical heterogeneity of BTS-M. Figure S31 shows the Raman spectra of BTS0.03 and BTS-M. The Raman images of BTS-M in Fig. 3d, e were derived from the features of the peaks at  $300$  and  $500 \text{ cm}^{-1}$ . The spatial variations in Raman signals are statistically significant. For comparison, the similar spatial signal images of BTS0.03 composition were depicted in Fig. S32. The highly variable peak positions and full widths at half maximum (FWHM) of BTS-M demonstrate the strong chemical fluctuation within a single grain<sup>28</sup>, which is absent in individual sample BTS0.03, and totally differs from the fluctuations in previously reported intergranular composites<sup>29,30</sup> or layered composites (2–2 type interactions)<sup>31–33</sup>. To further investigate the local interactions, the switching spectroscopy piezo-response force microscopy (SS-PFM) of BTS0.03 and BST-M was measured (Fig. S33). The SS-PFM curves of both samples display rectangular-shaped hysteresis loops with near  $180^\circ$  phase contrast, implying adequate polarization switching in both samples. However, BTS-M exhibits more violent fluctuations in the imprint  $\Delta V$  [determined as  $(|V_{+c}| + |V_{-c}|)$ , where  $V_{+c}$  and  $V_{-c}$  denote the positive and negative coercive biases, respectively] than BTS0.03 (Fig. 3f and Figs. S34–S36), confirming the chemical

fluctuation on the grain level<sup>34,35</sup>. The Raman and PFM measurements were performed on several grains for certainty (Figs. S37–S40).

So far, the extensive chemical inhomogeneity, which exists both beyond and inside grains, has been verified in BTS-M. Such three-dimensionally connected heterogeneity and sintering interdiffusion facilitate the formation of abundant interim regions, alleviating the chemical divergence between different BTSx units. Meanwhile, the observed heterogeneity reveals that the primary body of BTSx units is still well-reserved in BTS-M. The coexistence of different BTSx compositions assembles various polarization states, boosting the polar entropy at zero field. By affording polarization strength within the continuous phase transition temperatures, they also contribute to the widened EC temperature window of BTS-M.

#### Local structural characteristics

To better understand the underlying mesoscopic mechanisms contributing to the excellent EC properties, the local chemistry and microstructural details of BTS-M were explored using atomic-resolved transmission electron microscopy (TEM). Figure 4a–c shows the dark field TEM images of BTS-M. Multifarious domains featuring symbolic

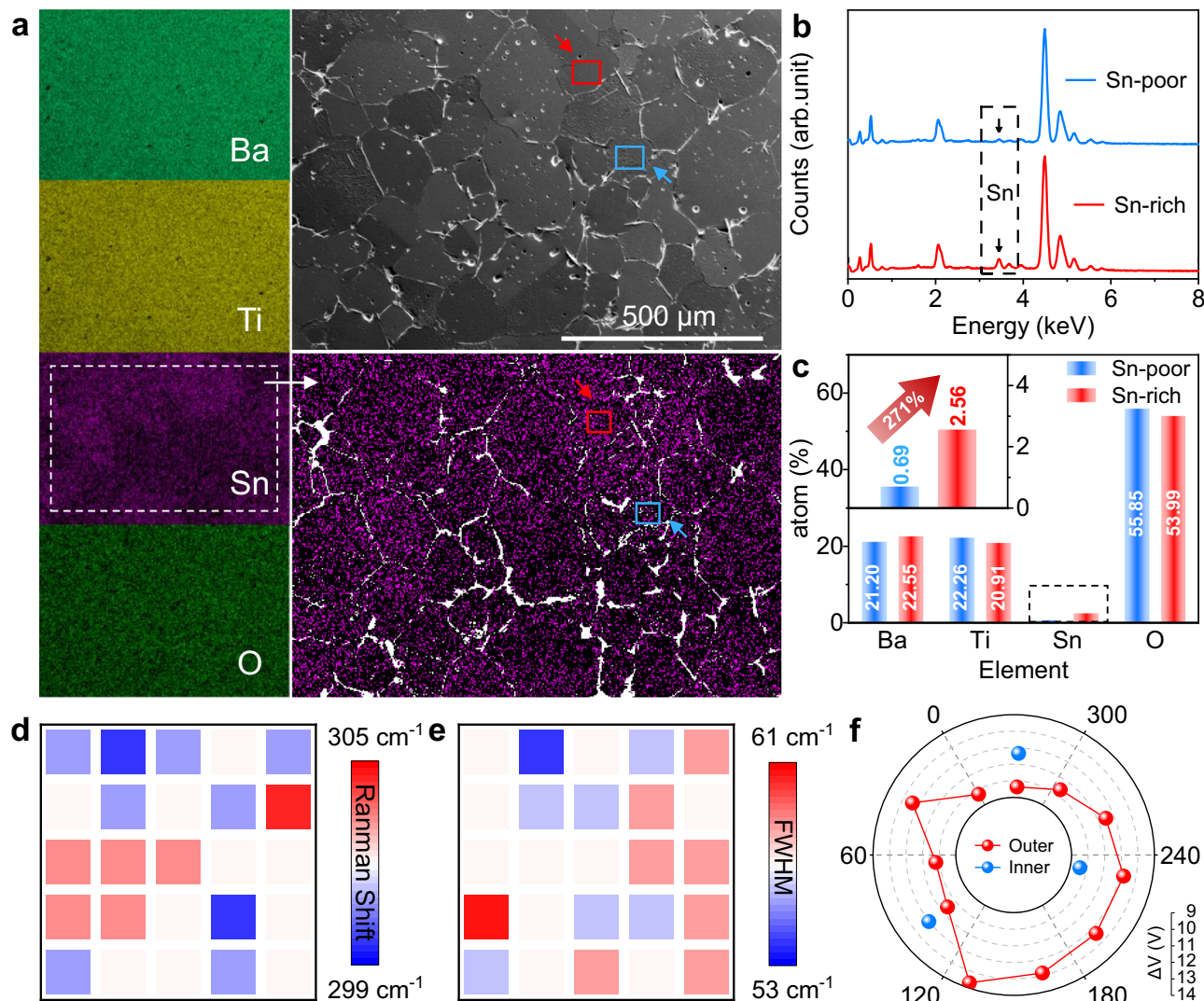


**Fig. 3 | Macroscale chemical heterogeneity of BTS-M.** **a** Scanning electron microscopy (SEM) and energy dispersive spectroscopy (EDS) images. **b** EDS spectra and **c** atomic percentages of the Sn-poor (blue-box) and Sn-rich (red-box) regions.

Spatial maps of **d** Raman shifts and **e** full widths at half maximum (FWHM). **f** Domain switching voltage of switching spectroscopy piezo-response force microscopy (SS-PFM) measurements.

stripes and nanosized or mottled structures were observed, where the striped submicron domains are interwoven with nanodomains in the sample. The domain size and pattern vary sharply in different regions, which may involve the local fluctuation of Sn<sup>36</sup>. In Fig. 4d–g, Figs. S41 and S42, EDS mappings illustrate the inhomogeneity of Sn in local areas, suggesting that chemical heterogeneity exists throughout the sample in multiple scales, that is, from microns to nanometers. For local characterization, the element fluctuations around interim regions were investigated through line scanning, and line profiles confirm the gradient variations of Sn and Ti elements (Fig. S43).

Figure S44 shows the electron diffraction pattern of BTS-M along the [110] zone axis. No superlattice diffraction is detectable, indicating no occurrence of octahedral tilts. The symmetries of the three phases [rhombohedral (R), orthorhombic (O), and tetragonal (T)] of BaTiO<sub>3</sub> can be differentiated through their lattice distortions, which can be considered as elongations of their parent cubic unit cells along one edge ([001]) of the T phase, along a face diagonal ([110]) of the O phase, and along a body diagonal ([111]) of the R phase. The spontaneous polarization ( $P_s$ ) directions are shown in Fig. 4h. Atomic-scale high-angle annular dark field (HAADF) image (Fig. 4i) indicates a nanoscale inhomogeneous state of polar vectors involving R, O, and T phases. It should be noted that the observed R, O, or T phase actually

consists of multiple compositions in BTS-M rather than one. Therefore, the actual polarization magnitude appears as a graded distribution in each phase. Meanwhile, benefited by the sintering interdiffusion, there are a large number of intermediate transition regions. These regions introduce interfacial energy (which includes electrostatic, elastic, and gradient energy), and this energy would compete with the bulk energy of the matrix, thereby lowering the Landau energy barrier between different phases and finally optimizing the EC performance of BTS-M.

## Discussion

Multiscale structural studies of BTS-M disclose a micron–nano heterogeneity stemming from the designed chemical inhomogeneity, which is distinct from the individual compositions<sup>37</sup> and is considered crucial for the EC performance of BTS-M (Fig. S45). Next, we performed in situ heating experiments with phase-field simulations to investigate the influence of chemical inhomogeneity in response to external fields.

As shown in Fig. 5a, the in situ TEM results reveal a rather stable domain configuration with wedge- and stripe-shaped domains during the heating experiments. The EDS analysis of the same area shows a varying distribution of Sn (Fig. S46), suggesting the local chemical heterogeneity, which can afford polarization change within a wide

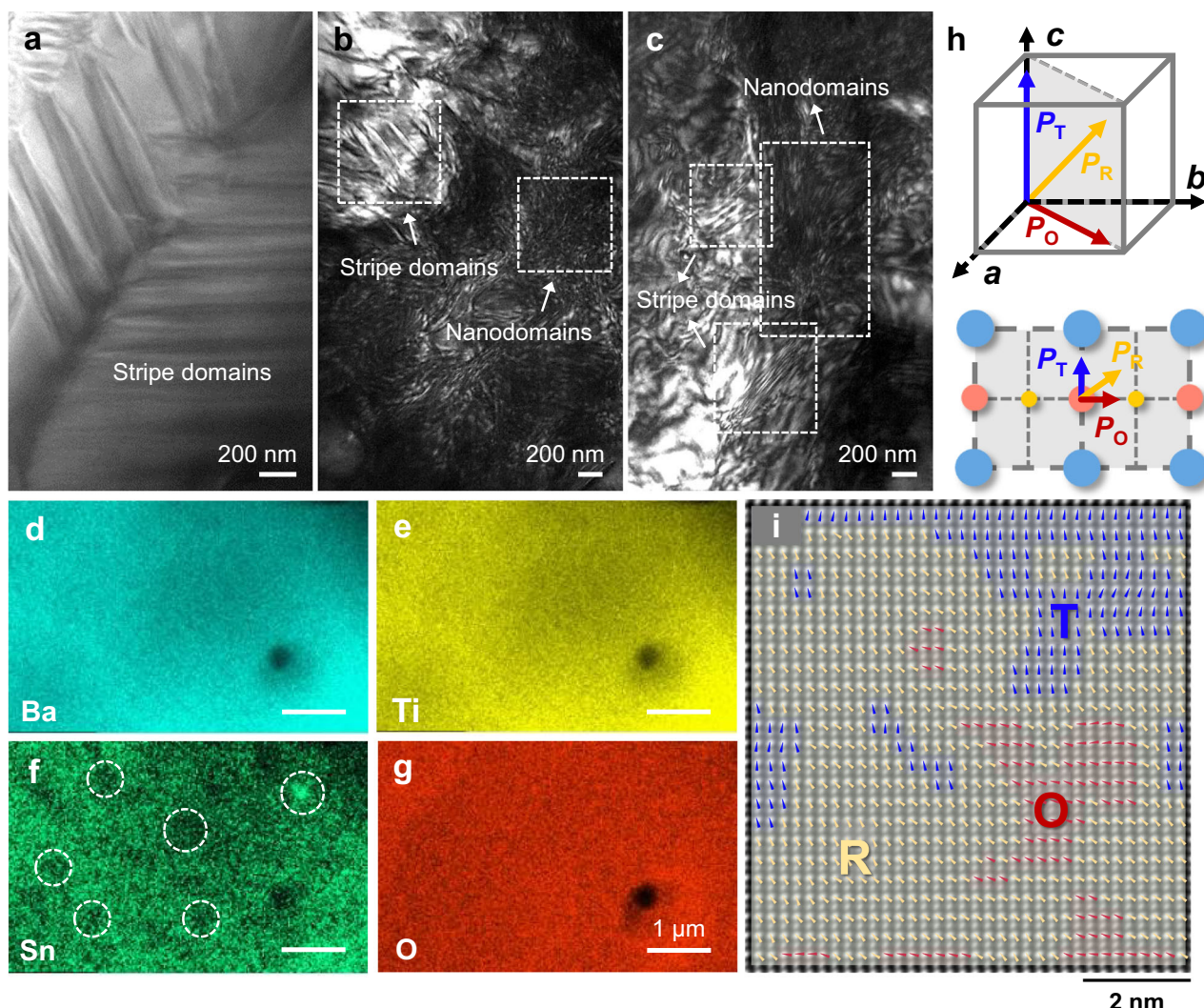


**Fig. 4 | Nano- and local-scale chemical heterogeneity of BTS-M.** **a–c** Dark field TEM images showing complex domain configurations. **d–g** EDS elemental mappings in a single grain. **h** Schematics of the  $\text{ABO}_3$  unit cell and its projection along

the [110] zone axis. **i** Cation-displacement vector map derived from the high-angle annular dark field (HAADF) lattice image. The white dashed circle in (f) marks the Sn-poor and Sn-rich regions.

temperature range and favor desired EC stability. To further clarify the functionality of chemical heterogeneity in the entire system, the evolutions of domain structures of BTS-M were simulated (Fig. 5b). In the virgin state with no applied  $E$ , BTS-M exhibits multi-symmetries involving ferroelectric R, O, and T phases, consistent with the microstructural observation in Fig. 4i. In addition, domains of various sizes are dispersed in BTS-M, indicating the differential polarization (strength and direction) that comes from the different BTS<sub>x</sub> compositions. Such a disordered state boosts the polar entropy of the system at zero field. When applying an  $E$ , domains respond instantly due to the 3D connection of chemical heterogeneity, which facilitates polarization rotation in the heterogeneous matrix. For EC effect, the adiabatic depolarization after removing  $E$  is more cared, where the entropy of the system transfers from thermal entropy to dipole entropy and the materials cool down<sup>3</sup>. In Fig. 5b, most domains of BTS-M can switch back when  $E$  is removed, suggesting the good recoverability of dipoles. Therefore, the large and flexible polarization change is offered synchronously in BTS-M, ultimately contributing to the superior EC performance.

In summary, we proposed a multiscale engineering strategy to optimize the EC performance of ferroelectric ceramics. A large  $\Delta T$  of 1.5 K and a high  $\Delta T/\Delta E$  of 0.375 K mm kV<sup>-1</sup> are synchronously achieved

under 40 kV cm<sup>-1</sup>, while the substantial  $\Delta T$  of more than 1.2 K is maintained within 30–50 °C. The outstanding EC performance originates from the designed multiscale heterogeneity, implemented by facilely mixing the equal-mass individual granules. We demonstrated that the three-dimensionally connected chemical heterogeneity boosts the polar entropy of the system. Additionally, the formed interim regions bridge different polarization states and introduce interfacial energy. This interfacial energy competes with the bulk energy of the matrix, thereby lowering the Landau energy barrier between different phases, finally availing the large  $\Delta T$  and high  $\Delta T/\Delta E$  under the low  $E$ . Our work provides a universal paradigm for designing other high-performance EC materials.

## Methods

### Sample preparation

BTS<sub>x</sub> ( $x = 0.03, 0.06, 0.09, 0.12$ ) individual powders were prepared by the conventional solid-state reaction method. The raw materials of barium carbonate ( $\text{BaCO}_3$ , 99.95%), titanium dioxide ( $\text{TiO}_2$ , 99.99%), and stannic oxide ( $\text{SnO}_2$ , 99.95%) were purchased from the Aladdin Biochemical Technology Co., Ltd (Shanghai, China) and weighed according to the stoichiometric ratio of individual composition, then subject to ball milling with ethanol as the medium. A 250 mL nylon jar

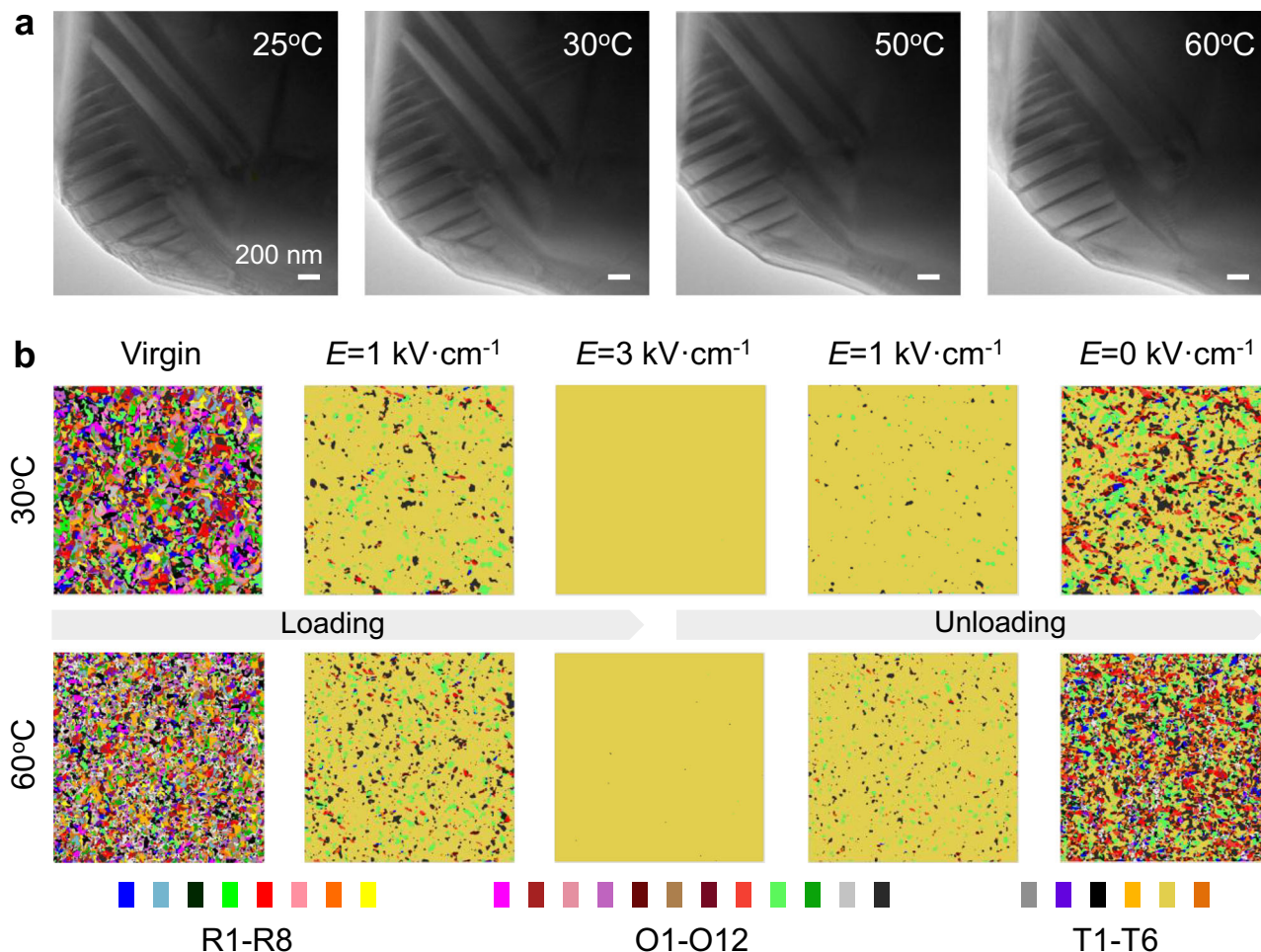


**Fig. 5 | Temperature- and  $E$ -dependent domain evolutions.** **a** In situ heating TEM observations. **b** domain structures simulated at different temperatures under different electric fields. The chromatic colors denote different ferroelectric phases with various spontaneous polarization directions.

was used for milling, along with zirconia grinding balls in diameters of 10 mm ( $\times 50$ ) and 5 mm ( $\times 200$ ). The ball-to-material mass ratio was controlled as ~10:1. The milling was operated at a rotation speed of 180 rpm for 24 h. The milled mixtures were dried and separately calcined at 1200 °C for 3 h. The four calcined powders were first granulated by adding polyvinyl alcohol (PVA) solution. Then, the granules were sieved to obtain 400  $\mu\text{m}$  granules. The 400  $\mu\text{m}$  granules of four individual compositions were well mixed together with the mass percentage of 1:1:1:1 and pressed into disks with 10 mm in diameter and 0.86 mm in thickness under a uniaxial pressure of 300 MPa for 5 min to fabricate BTS-M. Finally, all green samples were sintered in air at 1380 °C for 3 h.

### Structural measurements

The crystal structural information was obtained on a bulk X-ray diffractometer (Bruker D8 Advanced XRD, Bruker AXS Inc., Madison, WI, USA) with  $\text{Cu } K_{\alpha}$  radiation ( $\lambda = 1.5406 \text{ nm}$ ). The surface morphologies and element distributions in the samples were characterized using field-emission scanning electron microscopy (FE-SEM, JSM-7500: JEOL Ltd., Tokyo, Japan). Raman measurements were performed using a Raman spectrometer (Horiba iHR550, Japan) with a 532-nm excitation source. For FE-SEM and Raman measurements, the polished samples were thermally etched at 1280 °C for 10 min. The  $C_p$  measurements were performed using a differential scanning calorimeter (Discovery DSC 25, TA Instruments, New Castle, DE, USA) at a heating rate of 3 °C/min. The relative density was measured by the Archimedes method and repeated for three samples.

### TEM measurements

For TEM observation, specimens were prepared from the bulk materials by mechanical thinning and  $\text{Ar}^+$  ion milling in a Gatan PIPS II polishing system. The domain morphologies, EDS mappings, and atomic-scale imaging were examined on a field-emission TEM (JEM-F200, JEOL, Japan). The HAADF images were acquired on a spherical aberration-corrected scanning TEM (Hitachi HF5000). The convergence semi-angle was 20 mrad, the probe size was set to UHR mode, and the ensemble semi-angle was 60–320 mrad. The atomic positions were fitted in MATLAB code<sup>38,39</sup>. In situ heating TEM experiments were performed using a SmartSet Hot Stage controller (Gatan Model 901) with a heating rate of 10 °C/min.

### PFM measurements

Prior to PFM measurements, the samples were first polished and then subjected to thermal etching at 1280 °C for 10 min to make the grain boundaries visible. Subsequently, the local piezoelectric response was evaluated using the SS-PFM mode of a commercial atomic force microscope (MFP-3D, Asylum Research, USA) with a high-voltage module equipped.

### Electrical property measurements

Prior to electrical measurements, the as-sintered samples were coated with silver paste and then heated at 600 °C for 10 min to form electrodes on both sides. The  $\epsilon_r$ - $T$  curves of both unpoled and poled samples were measured in the frequency range of 0.1–100 kHz using a dielectric spectroscopy test system (TZDM-200–300, Harbin Julang Technology

Co., Ltd, Harbin, China). To prepare the poled samples, the unpoled samples with electrodes were poled at room temperature by applying a DC electric field of  $30 \text{ kV cm}^{-1}$  for 10 min in a silicone oil bath. The  $P$ - $E$  loops were acquired at the frequency of 1 Hz using an alternating-current triangular-bias electric field ranging from 5 to  $30 \text{ kV cm}^{-1}$  by a ferroelectric tester (aixACCT TF Analyzer 2000, Germany).

### Direct EC property measurements

For direct EC measurements, the gold electrode with a diameter of 2.5 mm was sputtered on one side of the sample, and on the other side, the gold electrode fully covers the sample. The overlap area was 2.5 mm in diameter. Therefore, the active electrode area of the sample is  $4.91 \text{ mm}^2$ , and the corresponding volume denotes the active part of the sample. The temperature change was recorded by an in situ calibrated calorimeter equipped with a typical heat flux sensor (RdF P/N 27134-3, Siemens, Germany). The unipolar pulse with a period of 35 s was applied by a synthesized function generator (Stanford Research Systems DS345). The rise and fall times of the pulse are 0.1 s. The measurement was repeated for 3 cycles for a single sample.

### Density functional theory (DFT) calculation

DFT calculations were conducted with the Perdew, Burke, and Ernzerhof for solid (PBEsol) exchange-correlation based on the generalized gradient approximation (GGA), which is implemented in the framework of Vienna ab initio Computational Simulation Package (VASP). The electron-ion interactions were described using the projector augmented wave (PAW), with plane-wave cutoffs set to 520 eV. The Ba 5s5p6s, Ti 3s3p3d4s, O 2s2p, and Sn 4d5s5p states were treated as valence electrons. A BTO structure with  $P4mm$  space group was used to generate a  $2 \times 2 \times 2$  supercell for Sn-doped BTO ( $\text{BaTi}_{0.875}\text{Sn}_{0.125}\text{O}_3$ ) model with 40 atoms. All the models were created using  $7 \times 7 \times 7$  Monkhorst-Pack k-point meshes. For electronic self-consistent iterations, the convergence conditions were set at  $10^{-5}$  eV, and the atomic coordinates were tuned until the Hellmann-Feynman forces were less than  $0.01 \text{ eV}/\text{\AA}$ . VASPkit, a pre-and post-processing tool for the VASP code, was utilized to prepare the necessary input files for the simulations.

### Phase-field simulations

The influences of chemical heterogeneity on the evolution of the domain structure were explored through phase-field modeling. The domain structures were characterized by the spatial distributions of spontaneous polarization  $\mathbf{P}$  ( $P_1, P_2, P_3$ ). The temporal evolutions of the polarizations were tracked using the time-dependent Ginzburg-Landau equation. In addition, the displacement field  $\mathbf{u}$  and electric displacement field  $\mathbf{D}$  were determined by solving the stress/electric equilibrium equations<sup>40</sup>

$$\frac{\partial P_i}{\partial t} = -L \frac{\delta F}{\delta P_j} + E_i^{\text{thermal}} \quad (1)$$

$$\frac{\partial}{\partial x_j} (\sigma_{ij}(r, t)) = 0 \quad (2)$$

$$\nabla \cdot \mathbf{D} = \rho_f \quad (3)$$

where  $L$  is a kinetic coefficient related to the domain-wall mobility,  $F$  is the total free energy of the system,  $\frac{\delta F}{\delta P_j}$  is the thermodynamic driving force of polarization evolution,  $\sigma_{ij}$  is the stress tensor,  $\rho_f$  is the free-charge density, and  $r$  and  $t$  denote the spatial coordinates and time, respectively.

The total free energy of a bulk system can be defined as:

$$F = F_{\text{bulk}}(P) + F_{\text{grad}}(P) + F_{\text{elastic}}(P) + F_{\text{elec}}(P, E) \\ = \int_V (f_{\text{bulk}} + f_{\text{grad}} + f_{\text{elastic}} + f_{\text{elec}}) dV \quad (4)$$

where  $F_{\text{bulk}}(P)$  is the bulk free energy,  $F_{\text{grad}}(P)$  is the domain-wall energy,  $F_{\text{elastic}}(P)$  is the elastic energy, and  $F_{\text{elec}}(P, E)$  is the electrostatic energy. Here,  $E$  is the applied static electric field. The terms  $f_{\text{bulk}}$ ,  $f_{\text{grad}}$ ,  $f_{\text{elastic}}$ , and  $f_{\text{elec}}$  are the corresponding energy densities.

The bulk free-energy density is expanded as a sixth-order polynomial:

$$f_{\text{bulk}} = \alpha_1 (P_1^2 + P_2^2 + P_3^2) + \alpha_{11} (P_1^4 + P_2^4 + P_3^4) + \alpha_{12} (P_1^2 P_2^2 + P_2^2 P_3^2 + P_1^2 P_3^2) \\ + \alpha_{111} (P_1^6 + P_2^6 + P_3^6) + \alpha_{112} [P_1^4 (P_2^2 + P_3^2) + P_2^4 (P_1^2 + P_3^2) + P_3^4 (P_1^2 + P_2^2)] \\ + \alpha_{123} P_1^2 P_2^2 P_3^2 \quad (5)$$

where  $\alpha_i$ ,  $\alpha_{ij}$ ,  $\alpha_{ijk}$  are the Landau parameters.

The elastic energy density is determined as

$$f_{\text{elas}} = \frac{1}{2} c_{ijkl} (\varepsilon_{ij} - \varepsilon_{ij}^0) (\varepsilon_{kl} - \varepsilon_{kl}^0) \quad (6)$$

where  $c_{ijkl}$  is the elastic stiffness tensor,  $\varepsilon_{ij}$  is the total strain, and  $\varepsilon_{ij}^0$  is the eigenstrain, calculated as  $\varepsilon_{ij}^0 = Q_{ijkl} P_k P_l$ , with  $Q_{ijkl}$  being the electrostrictive coefficient.

The gradient energy density is obtained as

$$f_{\text{grad}} = \frac{1}{2} G_{ijkl} P_{i,j} P_{k,l} \quad (7)$$

where  $G_{ijkl}$  is the gradient coefficient.

The electrostatic energy is expressed as

$$f_{\text{elec}} = -P_i(r) E_i(r) - \frac{1}{2} \varepsilon_0 \kappa_{ij}^b(r) E_i(r) E_j(r) \quad (8)$$

where  $\kappa_{ij}^b(r)$  is the background dielectric constant tensor,  $\varepsilon_0$  is the vacuum permittivity,  $E_i$  is the electric field component, and  $P_i$  is the polarization component<sup>41-43</sup>.

The simulation scale was  $256\text{dx} \times 256\text{dz}$ , where  $\text{dx}$  and  $\text{dz}$  are the grid scales (both equal to 4 nm). The equations were solved using the Fourier method. The detailed parameters of the  $\text{BaTi}_{0.3-x}\text{BaSnO}_3$  system were selected from refs. 22,31,44 and are listed below:

$$T_C = -271.7 \times 1.143x + 75.0 \\ \alpha_1 = (T - T_C) \times 4.124 \times 10^5 C^{-2} m^2 N \\ \alpha_{11} = -|1 - 5.833 \times 1.143x - 0.3| \times 4 \times 10^8 C^{-4} m^6 N \\ \alpha_{12} = 10^8 [-8.0|1 - 5.833 \times 1.143x - 0.3| - 5.833 \times 1.143x + 0.7 \\ + 0.01(T - 40.0)] C^{-4} m^6 N \\ \alpha_{111} = 12.94 \times 10^8 C^{-6} m^{10} N \\ \alpha_{112} = [12.94 \times 3.0 \times 10^8 - (1 - 5.833 \times 1.143x - 0.3) \times 10^8] C^{-6} m^{10} N \\ \alpha_{123} = [12.94 \times 6.0 \times 10^8 + (1 - 5.833 \times 1.143x - 0.3) \times 4.0 \times 10^8] C^{-6} m^{10} N \\ Q_{11} = 0.11 m^4 C^{-2}, Q_{12} = -0.045 m^4 C^{-2}, Q_{44} = 0.029 m^4 C^{-2} \\ S_{11} = 9.07 \times 10^{-12} m^2 N^{-1}, S_{12} = -3.186 \times 10^{-12} m^2 N^{-1}, S_{44} = 8.197 \\ \times 10^{-12} m^2 N^{-1}$$

The gradient energy coefficients were chosen as  $G_{11}/G_{110} = 1.0$ ,  $G_{12}/G_{110} = 0.0$ ,  $G_{44}/G_{110} = 0.5$ , where  $G_{110} = 7.04 \times 10^{-11} C^{-2} m^4 N$ . When  $x = 0$ , the potential function can produce R, O, and T phase transition structures. As  $x$  increases, the ferroelectric transition becomes a pure R phase.

### Data availability

The authors declare that the data supporting the findings of this study are available within the paper and its Supplementary Information files. More relevant data sets generated during and/or analyzed during the current study are available from the first authors and corresponding authors upon reasonable request. Source Data are provided within this paper. Source data are provided with this paper.

## References

1. Moya, X. & Mathur, N. D. Caloric materials for cooling and heating. *Science* **370**, 797–803 (2020).
2. Klinar, K. & Kitanovski, A. Thermal control elements for caloric energy conversion. *Renew. Sustain. Energy Rev.* **118**, 109571 (2020).
3. Valant, M. Electrocaloric materials for future solid-state refrigeration technologies. *Prog. Mater. Sci.* **57**, 980–1009 (2012).
4. Qian, X. S. et al. High-entropy polymer produces a giant electrocaloric effect at low fields. *Nature* **600**, 664–669 (2021).
5. Li, J. N. et al. High cooling performance in a double-loop electrocaloric heat pump. *Science* **382**, 801–805 (2023).
6. Wang, Z. Y. et al. Self-sustaining personal all-day thermoregulatory clothing using only sunlight. *Science* **382**, 1291–1296 (2023).
7. Acosta, M. et al. BaTiO<sub>3</sub>-based piezoelectrics: fundamentals, current status, and perspectives. *Appl. Phys. Rev.* **4**, 041305 (2017).
8. Li, J. N. et al. Large room-temperature electrocaloric effect in lead-free BaHf<sub>x</sub>Ti<sub>1-x</sub>O<sub>3</sub> ceramics under low electric field. *Acta Mater.* **115**, 58–67 (2016).
9. Sanlialp, M. et al. Direct measurement of electrocaloric effect in lead-free Ba(Sn<sub>x</sub>Ti<sub>1-x</sub>)O<sub>3</sub> ceramics. *Appl. Phys. Lett.* **111**, 173903 (2017).
10. Hanani, Z. et al. Thermally-stable high energy storage performances and large electrocaloric effect over a broad temperature span in lead-free BCZT ceramic. *RSC Adv.* **10**, 30746–30755 (2020).
11. Yang, J. L., Zhao, Y., Lou, X. J., Wu, J. G. & Hao, X. H. Synergistically optimizing electrocaloric effects and temperature span in KNN-based ceramics utilizing a relaxor multiphase boundary. *J. Mater. Chem. C* **8**, 4030–4039 (2020).
12. Novak, N., Weyland, F. & Rossetti, G. A. Electrocaloric properties and caloric figure of merit in the ferroelectric solid solution BaZrO<sub>3</sub>–BaTiO<sub>3</sub> (BZT). *J. Eur. Ceram. Soc.* **41**, 1280–1287 (2021).
13. Xiao, W. R. et al. Significant enhancement of electrocaloric effect in ferroelectric polycrystalline ceramics through grain boundary barrier engineering. *Adv. Funct. Mater.* **34**, 2405241 (2024).
14. Li, F. et al. Superior electrocaloric performance enabled by highly robust monomorphic ferrodistortion in NaNbO<sub>3</sub>-based relaxor. *Adv. Funct. Mater.* **35**, 2418534 (2025).
15. Zhao, C. L., Huang, Y. L. & Wu, J. G. Multifunctional barium titanate ceramics via chemical modification tuning phase structure. *InfoMat* **2**, 1163–1190 (2020).
16. Qian, X. S. et al. Giant electrocaloric response over a broad temperature range in modified BaTiO<sub>3</sub> ceramics. *Adv. Funct. Mater.* **24**, 1300–1305 (2024).
17. Luo, Z. D. et al. Enhanced electrocaloric effect in lead-free BaTi<sub>1-x</sub>Sn<sub>x</sub>O<sub>3</sub> ceramics near room temperature. *Appl. Phys. Lett.* **105**, 102904 (2014).
18. Zhang, X. et al. Large electrocaloric effect in Ba(Ti<sub>1-x</sub>Sn<sub>x</sub>)O<sub>3</sub> ceramics over a broad temperature region. *AIP Adv.* **5**, 047134 (2015).
19. Ma, X. Y. et al. Giant electrocaloric effect and high-field electrostrictive properties in Ba(Ti<sub>1-x</sub>Sn<sub>x</sub>)O<sub>3</sub> ceramics. *Ceram. Int.* **49**, 18517–18524 (2023).
20. Yasuda, N., Ohwa, H. & Asano, S. Dielectric properties and phase transitions of Ba(Ti<sub>1-x</sub>Sn<sub>x</sub>)O<sub>3</sub> solid solution. *Jpn. J. Appl. Phys.* **35**, 5099–5103 (1996).
21. Shi, T., Xie, L., Gu, L. & Zhu, J. Why Sn doping significantly enhances the dielectric properties of Ba(Ti<sub>1-x</sub>Sn<sub>x</sub>)O<sub>3</sub>. *Sci. Rep.* **5**, 8606 (2015).
22. Yao, Y. G. et al. Large piezoelectricity and dielectric permittivity in BaTiO<sub>3</sub>-xBaSnO<sub>3</sub> system: the role of phase coexisting. *EPL* **98**, 27008 (2012).
23. Abe, T. et al. Visualization of spontaneous electronic polarization in Pb ion of ferroelectric PbTiO<sub>3</sub> by synchrotron-radiation x-ray diffraction. *Appl. Phys. Lett.* **117**, 252905 (2020).
24. Li, F. et al. The origin of ultrahigh piezoelectricity in relaxor-ferroelectric solid solution crystals. *Nat. Commun.* **7**, 13807 (2016).
25. Li, F. et al. Ultrahigh piezoelectricity in ferroelectric ceramics by design. *Nat. Mater.* **17**, 349–354 (2018).
26. Wei, X. W. et al. Novel 3-3-like heterostructure engineering enables BaTiO<sub>3</sub>-based ferroelectric ceramics with superior electrocaloric performance. *Acta Mater.* **285**, 120674 (2025).
27. Zhang, J. et al. Semiconductor/relaxor O-3 type composites without thermal depolarization in Bi<sub>0.5</sub>Na<sub>0.5</sub>TiO<sub>3</sub>-based lead-free piezoceramics. *Nat. Commun.* **6**, 6615 (2015).
28. Reyes-Montero, A. et al. Confocal Raman microscopy, synchrotron X-ray diffraction, and photoacoustic study of Ba<sub>0.85</sub>Ca<sub>0.15</sub>Ti<sub>0.90</sub>Zr<sub>0.10</sub>O<sub>3</sub>: understanding structural and microstructural response to the electric field. *ACS Appl. Electron. Mater.* **3**, 2966 (2021).
29. Groh, C. et al. Relaxor/ferroelectric composites: a solution in the quest for practically viable lead-free incipient piezoceramics. *Adv. Funct. Mater.* **24**, 356 (2014).
30. Li, B. et al. Constructing relaxor/ferroelectric pseudocomposite to reveal the domain role in electrostrain of bismuth ferrite-barium titanate-based ceramics. *ACS Appl. Mater. Interfaces* **14**, 18713 (2022).
31. Gao, J. H. et al. Laminated modulation of tricritical ferroelectrics exhibiting highly enhanced dielectric permittivity and temperature stability. *Adv. Funct. Mater.* **29**, 1807162 (2019).
32. Yin, R. W. et al. Emergent enhanced electrocaloric effect within wide temperature span in laminated composite ceramics. *Adv. Funct. Mater.* **32**, 108182 (2021).
33. Lin, W. K. et al. Broadening the operating temperature span of the electrocaloric effect in lead-free ceramics via creating multi-stage phase transitions. *J. Mater. Chem. A* **12**, 16438 (2024).
34. Zhang, M. H. et al. Determination of polarization states in (K,Na)NbO<sub>3</sub> lead-free piezoelectric crystal. *J. Adv. Ceram.* **9**, 204 (2020).
35. Jesse, S., Lee, H. N. & Kalinin, S. V. Quantitative mapping of switching behavior in piezoresponse force microscopy. *Appl. Phys. Lett.* **77**, 073702 (2006).
36. Thong, H. C. et al. Domain engineering in bulk ferroelectric ceramics via mesoscopic chemical inhomogeneity. *Adv. Sci.* **9**, 2200998 (2022).
37. Jiang, Z. J. et al. Phase evolution and local piezoelectric response of Sn-doped BaTiO<sub>3</sub> ceramics. *Phys. Status Solidi A* **219**, 2200344 (2022).
38. De Backer, A., Van den Bos, K. H. W., Van den Broek, W., Sijbers, J. & Van Aert, S. StatSTEM: An efficient approach for accurate and precise model-based quantification of atomic resolution electron microscopy images. *Ultramicroscopy* **171**, 104 (2016).
39. Van Aert, S. et al. Advanced electron crystallography through model-based imaging. *IUCrJ* **3**, 71 (2016).
40. Shi, X. M., Wang, J., Xu, J. W., Cheng, X. W. & Huang, H. B. Quantitative investigation of polar nanoregion size effects in relaxor ferroelectrics. *Acta Mater.* **237**, 118147 (2022).
41. Marvan, M. & Fousek, J. Electrostatic energy of ferroelectrics with nonhomogeneous distributions of polarization and free charges. *Phys. Status Solidi B* **208**, 523 (1998).
42. Vorotilahin, I. S. et al. General approach for the description of size effects in ferroelectric nanosystems. *Acta Mater.* **137**, 85 (2017).
43. Eliseev, E. A. & Morozovska, A. N. General approach for the description of size effects in ferroelectric nanosystems. *J. Mater. Sci.* **44**, 5149 (2009).
44. Gao, J. H. et al. Enhancing dielectric permittivity for energy-storage devices through tricritical phenomenon. *Sci. Rep.* **7**, 40916 (2017).

## Acknowledgements

This work is supported by the National Natural Science Foundation of China [Grant Nos. U23A20567 (J.W.) and 12204327 (X.L.)], the Natural Science Foundation of Sichuan Province [Grant Nos. 2023NSFSC0967 (X.L.) and 2024NSFJQ0025 (J.W.)], the Fundamental Research Funds for the Central Universities [Grant No. YJ202483 (J.W.)], the Postdoctoral Fellowship Program of China Postdoctoral Science Foundation [Grant No. GZB20250773 (J.W.)], and Sichuan University postdoctoral interdisciplinary Innovation Fund. The authors thank Dr. Chunlin Zhao (Fuzhou

University) for fruitful discussions, Ms. Hui Wang (Analytical & Testing Center of Sichuan University) for the FE-SEM measurements, and Dr. Xiaoqin Ke (Xi'an Jiaotong University) for providing the LGD parameters.

## Author contributions

X.W., X.L., and J.W. conceived the idea of this work. X.W. and B.L. fabricated the ceramic samples. X.W. performed the XRD, Raman, and PFM measurements. K.Z. and Z.F. performed the TEM investigation. X.S. and H.H. performed the phase-field simulations. G.L. and G.Z. performed the direct EC measurements. All authors discussed the results. X.W., X.L., and J.W. wrote the manuscript, and all authors participated in its modification. X.L. and J.W. guided the projects.

## Competing interests

The authors declare no competing interests.

## Additional information

**Supplementary information** The online version contains supplementary material available at <https://doi.org/10.1038/s41467-025-63909-x>.

**Correspondence** and requests for materials should be addressed to Houbing Huang, Xiang Lv or Jiagang Wu.

**Peer review information** *Nature Communications* thanks Lovro Fulanović, Limei Jiang, and the other anonymous reviewer(s) for their contribution to the peer review of this work. A peer review file is available.

**Reprints and permissions information** is available at <http://www.nature.com/reprints>

**Publisher's note** Springer Nature remains neutral with regard to jurisdictional claims in published maps and institutional affiliations.

**Open Access** This article is licensed under a Creative Commons Attribution-NonCommercial-NoDerivatives 4.0 International License, which permits any non-commercial use, sharing, distribution and reproduction in any medium or format, as long as you give appropriate credit to the original author(s) and the source, provide a link to the Creative Commons licence, and indicate if you modified the licensed material. You do not have permission under this licence to share adapted material derived from this article or parts of it. The images or other third party material in this article are included in the article's Creative Commons licence, unless indicated otherwise in a credit line to the material. If material is not included in the article's Creative Commons licence and your intended use is not permitted by statutory regulation or exceeds the permitted use, you will need to obtain permission directly from the copyright holder. To view a copy of this licence, visit <http://creativecommons.org/licenses/by-nc-nd/4.0/>.

© The Author(s) 2025